High-Sensitivity Biochemical Sensor Based on Cylindrical Nano-Metal Particles Array

Yue Jing He

***Abstract*—This work proposes a novel localized surface plasmon resonance (LSPR) biochemical sensor featuring high sensitivity and a high resolution. The sensor was divided into two subcomponents according to their distinct functions; namely, single-mode fiber and metal array. Single-mode fibers located on the left and right sides of the sensors function as the input and output for optical fiber signals. A metal array comprising an arrangement of cylindrical nanometal particles served as the detection area of the sensor. To effectively reduce the memory capacity and calculation time, two innovative techniques (i.e., object meshing and boundary meshing) were integrated with the finite element method. With the area of the triangular elements used as a basis, the object boundary, small object, medium object, and large objects were meshed at a ratio of 1:8:160:1600. The improved numerical simulation methods and six design procedures were adopted to develop and analyze the proposed LSPR biochemical sensor. The results show that the novel LSPR biochemical sensor outperformed two current high-performance biochemical sensors and provided additional advantages such as short length (approximately 430 μm), high resolution (approximately –120 dB), and high sensitivity (approximately 127 604 nm/RIU).**

***Index Terms*—Boundary meshing method, eigenmode expansion method, finite element method, object meshing method, optical biochemical LSPR fiber sensors, perfectly matched layer, perfectly reflecting boundary condition.**

I. Introduction

In recent years, the optical properties of surface plasmon resonance (SPR) have been widely utilized in various fields. SPR waves are physical phenomena characterized by the collective oscillation of free electrons. This phenomenon is described as follows: In some metal materials (e.g., gold, silver, and copper), free electrons can absorb energy from incident rays of a particular wavelength; when this occurs, the free electrons on the surface of the metals oscillate collectively [1]–[2]. According to their transmission ability, SPR waves can be categorized according to whether they possess transmission ability. Regarding the SPR waves that possess this ability, once a metal is excited by an incident ray, energy propagates along the surface of the metal. This type of SPR wave is commonly used in such fields as biological sensing, genetic engineering, and chemical sensing [3]–[12]. By contrast, SPR waves without transmission ability are primarily found in nanometal particles; because these particles are so small, they have no transmission ability. When free electrons absorb incident rays of a particular wavelength, collective oscillation occurs both on the surface of the nanometal particles and also between the particles. This type of SPR wave is also called a localized SPR (LSPR) wave. According to the SPR principle, the higher the number of locations in a sensor that can be used to excite a SPR wave, the more able the sensor is in detecting changes in the refractive index of an analyte [13]. LSPR biochemical sensors outperform general SPR biochemical sensors. In addition, LSPR biochemical sensors have been frequently used in research related to biochemical and environmental sensing [14]–[21]. Using the optical properties of LSPR, this study developed a novel LSPR biochemical sensor featuring high sensitivity and a high resolution.

When designing and investigating elements with a large and periodic structure, the combination of the finite element method (FEM) and the eigenmode expansion method (EEM) can be used as a powerful numerical simulation method. This combined method was developed by the author of this study, who has also published several studies on high-performance SPR biochemical sensors [13], [22]. The core concept of the FEM is based on the method of Fourier series expansion. Fourier series expansion calculations require a sufficient number of expansion bases to avoid large errors. The FEM is also affected by this problem. Because arbitrary waveguide structures contain many discrete guided modes and continuous radiation modes, all of the continuous radiation modes cannot be included in numerical simulations and errors are inevitable. In this study, the perfectly matched layer (PML) and perfectly reflecting boundary (PRB) were integrated with the FEM to minimize the gap between simulation results and actual application [13]. However, a considerable drawback of using the improved FEM is that it uses uniform triangular elements to perform meshing. Because designing and researching SPR sensors inevitably involves nanometal particles and nanoscale waveguides, effective control of the meshing resolution is crucial for minimizing the simulation time and required memory capacity. Therefore, in this study, the object meshing method (OMM) and the boundary meshing method (BMM) were used to improve the FEM meshing technique.

The remainder of this paper is organized as follows. Section II presents the novel LSPR biochemical sensor and describes the geometric components, material properties, array arrangements of the nanometals, and operation principles of the sensors by using 2-D and 3-D images. The principles of optics governing LSPR posit that a sensor with more locations for exciting LSPR

Manuscript received April 8, 2015; revised June 5, 2015 and June 21, 2015; accepted June 22, 2015. Date of publication July 31, 2015; date of current version August 3, 2015. This work was supported by the Ministry of Science and Technology (MOST 103-2221-E-167-001 and MOST 104-2221-E-167-013-MY2) of Taiwan.

The author is with the Department of Electronic Engineering, National Chin-Yi University of Technology, Taichung 41170, Taiwan (e-mail: yuejing@ncut.edu.tw).

Color versions of one or more of the figures in this paper are available online at http://ieeexplore.ieee.org.

Digital Object Identifier 10.1109/JLT.2015.2448935

0733-8724 © 2015 IEEE. Personal use is permitted, but republication/redistribution requires IEEE permission.
See http://www.ieee.org/publications_standards/publications/rights/index.html for more information.

waves is more able to detect changes in the refractive index of an analyte [13]. Therefore, the number of nanometal particles is also investigated in this chapter. In addition, relevant production techniques are investigated to ensure the successful creation of the novel LSPR biochemical sensor.

Section III briefly introduces the FEM and explains its role and function in designing and researching the novel LSPR biochemical sensor. During the calculation process, discrete radiation modes were included to minimize the difference between the simulations and actual application. The principles of PML and PRB are briefly described in this chapter to ensure that the reader understands these methods, and OMM and BRM are proposed to overcome the drawback of using uniform triangular elements in the improved FEM. Accordingly, a detailed explanation and discussion of these two methods is provided. Because of the limited memory capacity of servers and the lengthy calculation times when performing numerical simulations, errors are inevitable; therefore, this chapter also provides a detailed and specific description of the types of error that can be created through using the FEM. An error-checking mechanism previously proposed by the author was adopted in this study, in which the FEM meshing resolution was required to produce an orthogonality of less than –40 dB in the obtained modes [13], [22]. This chapter also investigates whether all of the objects and parameters used in creating the novel sensor could excite localized surface plasmons. Finally, the 2-D power distribution map of the core mode (HE_{11}), discrete LSPR wave, and discrete radiation modes obtained using the FEM are presented. The figures show that SPR waves occurred on and in between the nanometal particles; such an optical property is the primary reason for the novel LSPR biochemical sensor's high sensitivity and resolution.

Section IV briefly introduces the EEM and its role in researching and designing the novel LSPR biochemical sensor. When designing and researching elements with a large and periodic structure, the combination of the FEM and EEM is not only a powerful numerical simulation method, but it is currently the only numerical simulation method available. The FEM and Fourier series expansion work in the same manner in optical physics as they do in pure mathematics; in mathematical operations, a sufficient number of Fourier series expansion bases must be used to avoid errors. Consequently, EEM is faced with the same problem. Therefore, an error-checking mechanism previously proposed by the author was used. Specifically, when performing EEM calculations, a sufficient number of modes must be used to control the overall energy consumption of the biochemical sensor at less than –40 dB [13], [22].

Section V describes the approach to designing and researching the novel LSPR biochemical sensor. Based on the theories described in Sections III and IV, four procedures and two verification mechanisms are proposed for analyzing the performance of the proposed sensor. In addition, to ensure that LSPR waves can be excited by the sensor, the core mode was entered through the input terminal of the sensor before the calculations were made, and a power distribution map was plotted on the *y*-*z* plane. To confirm the superior performance of the proposed sensor, two key indices (i.e., sensitivity and resolution) were calculated using the spectral properties of the sensor. Finally, to explain the novel sensor's exceptionally high performance, the sensor is compared with two previous sensor structures, and the results are discussed. The two sensors are a high-performance LSPR biochemical fiber sensor [13] and a D-shape LSPR fiber sensor based on nanometal strips [22].

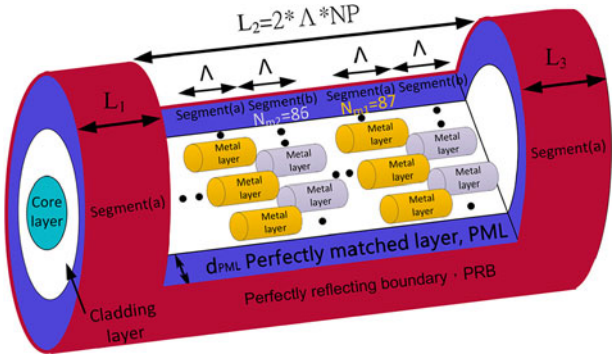

Fig. 1. 3-D image of the sensor structure.

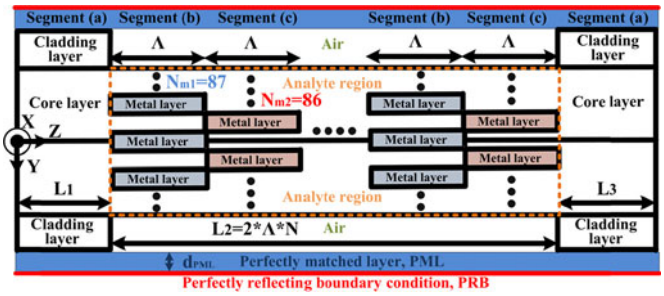

Fig. 2. 2-D diagram of the sensor structure (*y*-*z* plane).

Section VI briefly reviews the OMM, BMM, four design procedures, two verification mechanisms, and framework of the proposed LSPR biochemical sensor. The design and simulation results presented in Section V confirm that the novel LSPR biochemical sensor features superior performance and advantageous properties such as a short length (approximately 430 μm), high resolution (approximately –120 dB), and high sensitivity (approximately 127 604 nm/RIU).

II. Novel LSPR Biochemical Sensor

Figs. 1–3 show the geometry of the novel LSPR biochemical sensor. Fig. 1 is a 3-D schematic diagram of the sensor structure, Fig. 2 is a 2-D schematic diagram of the sensor structure on the *y*-*z* plane, and Fig. 3 is a 2-D schematic diagram of the sensor structure on the *x*-*y* plane.

The sensor comprised two subcomponents: single-mode fibers and a metal array. Segment (a) of Figs. 2 and 3 show the single-mode fibers located on the left and right sides of the sensors, which are responsible for the input and output of optical fiber signals. Segments (b) and (c) in Figs. 2 and 3 show the metal array as an arrangement of cylindrical nanometal particles, which serve as the detection area of the sensor. The two metal arrays were produced using the same method: First, the optical fiber was etched down to the core layer, forming a D-shaped structure. Subsequently, the D-shaped structure was plated with

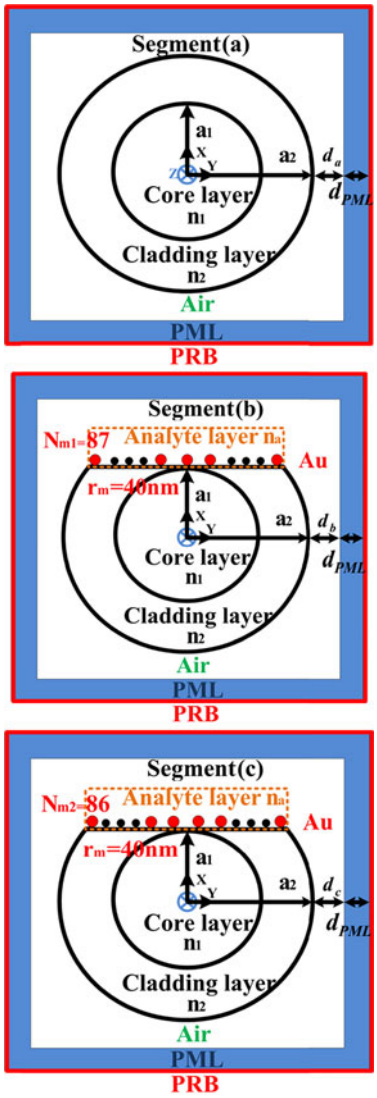

Fig. 3. 2-D diagram of the sensor structure (*x*-*y* plane).

gold cylindrical nanometal arrays. The cylindrical nanometal arrays were arranged with the center of the core layer as the reference line, with the arrays positioned on the left and right sides of the reference line; the duty cycle of the arrays was 0.5. Segments (b) and (c) differ in their position relative to the central reference line: for Segment (b), an odd number of arrays was arranged symmetrically to the left and right sides of the reference line, whereas for Segment (c), an even number of arrays was arranged symmetrically along the reference line. In Segments (b) and (c), the number of cylindrical nanometal particles, denoted as N_{m1} and N_{m2}, respectively, was 87 and 86, respectively. The length of Segments (b) and (c) was set equal to the length of the cylindrical nanometal particles ($\Lambda = 0.1\ \mu$m).

The structures and material parameters of the novel LSPR biochemical sensor are shown below: $\mathrm{a_1} = 2.25\ \mu$m, $\mathrm{a_2} = 7.25\ \mu$m, $\mathrm{r_m} = 0.04\ \mu$m, $\mathrm{d_{PML}} = 0.825\ \mu$m, $\mathrm{n_1} = 1.454$, $\mathrm{n_2} = 1.43$, $\mathrm{n_a} = 1.33$, $\mathrm{N_{m1}} = 87$, $\mathrm{N_{m2}} = 86$, $\Lambda = 0.1\ \mu$m, $L_1 = 30\ \mu$m, $\mathrm{L_3} = 30\ \mu$m, NP = 1850, $L_2 = \mathrm{NP}^*2^*\ \Lambda = 370\ \mu$m, $\mathrm{d_a} = 6\ \mu$m, $\mathrm{d_b} = 6\ \mu$m, $\mathrm{d_c} = 6\ \mu$m, and $\mathrm{n_m} = 0.56246309 + j9.840798407$ (at $\lambda = 1550\ \mu$m). The length of the sensor is $\mathrm{L} = \mathrm{L_1} + \mathrm{L_2} + \mathrm{L_3} = 430\ \mu$m. The refractive index of the analyte is denoted as $\mathrm{n_a}$, and the metal material was composed of gold. The relationship between the refractive index and wavelength was obtained from a previous study [22]. In the proposed novel, highly sensitive biochemical sensor, the sensing region consists of Segments (b) and (c), which are arranged in a 0.5 duty cycle. The total number nanogold particles in Segments (b) and (c) were 87 and 86, respectively. In addition, the total number for Segments (b) and (c) were 1850. Therefore, according to the preceding explanation, the total number of nanogold particles in the sensor was 320 050 ((87 + 86) × 1850). To excite LSPR waves, previous studies have indicated that nanometals must have a cross-sectional size of 20–70 nm. Therefore, in this study, the r_m of the novel LSPR biochemical sensor was set at 0.04 μm. A series of tests confirmed that the length of the cylindrical nanometal particles (Λ) was 0.1 μm. To fabricate the novel LSPR biochemical sensor, current production techniques were investigated; among the relevant production techniques, the electrochemical and photochemical reduction methods in aqueous surfactant media, porous alumina templates, polycarbonate membrane templates, and carbon nanotube templates were determined to be the most suitable for fabricating the proposed sensor [23].

III. Finite Element Method

The FEM is a powerful numerical calculation method for locating guided modes along a cross-section of waveguides of any shape. The FEM incorporates the variational principle, domain meshing, and interpolation as core methods [24]–[28]. Mathematically, when solving partial differential equations with boundary conditions, all mathematical solutions are orthogonal; in other words, the mathematical solutions have an orthogonality of 1 only with themselves, and the orthogonality between any two mathematical solutions is 0. According to the optical waveguide principle, in an arbitrary waveguide structure, complete modal solutions must contain both discrete guided modes and continuous radiation modes [13], [29]–[36]. When performing numerical simulations, including all of the continuous radiation modes is impossible because the number of modes is considerably high; consequently, errors are inevitable when using the FEM to solve the modes. To address this problem, the authors of this study proposed a method from their previous study, in which PML and PRB were integrated with the FEM [13], [36]. Because the PRB can be used to convert continuous radiation modes into discrete radiation modes, which causes a loss of energy when contact is made with the PMLs, a closed simulation space can be transformed into an open space, minimizing the difference between the simulation results and actual application. Based on the above interpretation, the scale of $\mathrm{d_a}$, $\mathrm{d_b}$, and $\mathrm{d_c}$ cannot be too small to influence the guided modes. In addition, in order to reduce the cost of the simulation time and memory, the scale of $\mathrm{d_a}$, $\mathrm{d_b}$, and $\mathrm{d_c}$ also cannot be too large. These three parameters were tested repeatedly. Finally, $d_a = 6\ \mu$m, $\mathrm{d_b} = 6\ \mu$m, and $\mathrm{d_c} = 6\ \mu$m were used in this novel sensor. Regarding the meshing resolution, the improved FEM has a serious

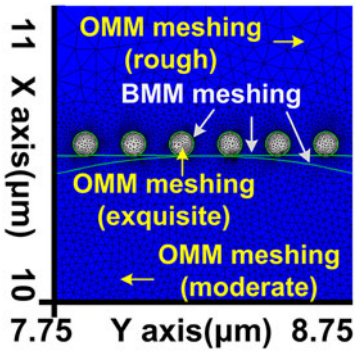

Fig. 4. Grid sizes of the BMM and the OMM.

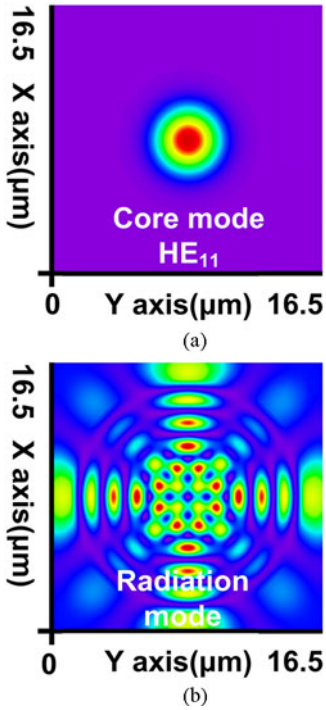

Fig. 5. 2-D image of the power distribution of Segment (a); (a) core mode (HE_{11}); and (b) discrete radiation mode.

problem resulting primarily from the FEM employing a meshing technique in which uniform triangular elements are used. Many biochemical sensors contain nanoscale metal particles and microscale waveguides. Given that the meshing technique uses uniform triangular elements, a considerable amount of memory and calculation time is wasted when performing meshing and calculations while ensuring that the nanometals achieve a favorable meshing resolution. Therefore, when performing calculations with the FEM, controlling of meshing resolution is crucial. To solve this problem, this study adopted the OMM and BMM [36]. The primary function of the OMM is to provide a means for designers to assign an appropriate but dynamic number of meshing triangles and resolutions to different sensor components. The primary function of the BMM is to provide a higher meshing resolution for the boundaries between the

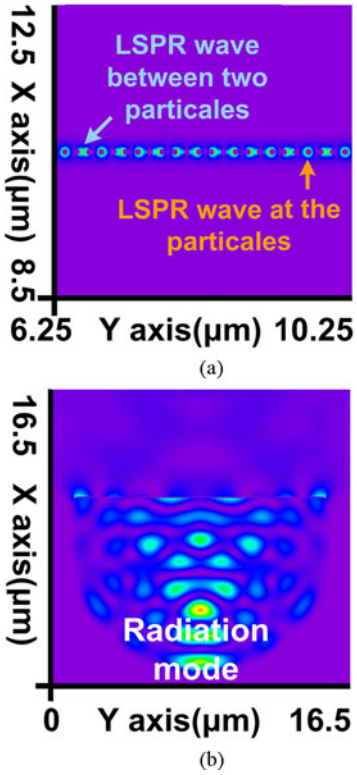

Fig. 6. 2-D image of the power distribution of Segment (b); (a) LSPR wave; and (b) discrete radiation mode.

objects in a sensor, enabling the FEM to be used to locate objects more accurately. This enables the accurate material parameters of the various objects to be used.

The proposed LSPR biochemical sensors could be divided into four structure types according to their object boundary and size (i.e., small, medium, or large). Based on the detailed descriptions provided above, and the area of the triangular element as the meshing reference, the object boundary, small object, medium object, and large objects were meshed at a ratio of 1:8:160:1600. Fig. 4 shows the meshing result. The figure shows that the BMM produced the smallest meshed grids for all object boundaries. Conversely, the OMM used the geometric sizes as the meshing standard, and the metal particles, core layer, and cladding layer were meshed into sizes described as small (exquisite), medium (moderate), and large (rough) [36].

Fig. 5 shows the results of the guided modes in Fig. 3(a), which were solved using the improved FEM; Fig. 5(a) and (b) respectively show the core mode (HE_{11}) and discrete radiation mode in Segment (a). Fig. 6 shows the results of the guided modes shown in Fig. 3(b), which were also solved using the improved FEM; Fig. 6(a) and (b) respectively present the discrete LSPR wave and discrete radiation mode in Segment(b). Fig. 6(a) shows that that the SPR wave exists both in the cylindrical nanometal particles and between them. Fig. 7 shows the results of the guided modes in Fig. 3(c), which were solved using the improved FEM; Fig. 7(a) and (b) respectively show the discrete LSPR wave and discrete radiation mode in Segment(c). The SPR phenomenon in Segment (b) also appears in Fig. 7(a).

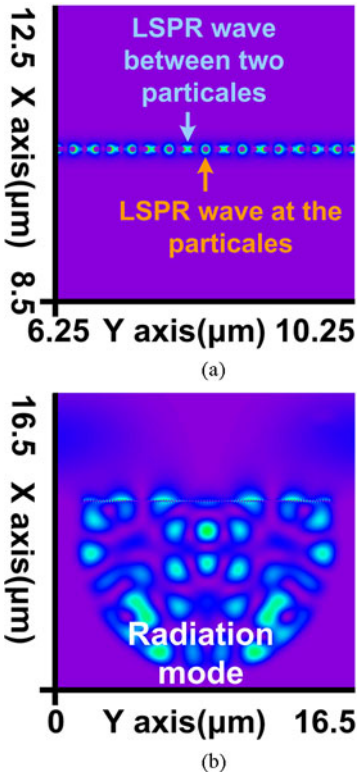

Fig. 7. 2-D image of the power distribution of Segment (c); (a) LSPR wave; and (b) discrete radiation mode.

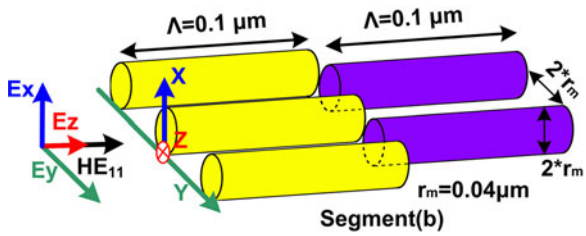

Fig. 8. Cylindrical nanometal array of HE_{11} in Segment (b), which was used to excite the LSPR wave.

According to the physical properties of the LSPR, the higher the number of locations of an SPR wave that can be excited, the more able a sensor is for detecting changes in the concentration of analytes; this is the primary reason for the high sensitivity exhibited in the proposed LSPR biochemical sensor. Fig. 8 shows the cylindrical nanometal arrangement in Segment (b) and Fig. 6(a) shows a 2-D image of the power distribution of an excited LSPR wave. Fig. 8 confirms that E_x and E_y, which are electric field components of HE_{11}, excited a 40-nm-radius dipole-like LSPR wave on the metal cylinder. A similar physical phenomenon appears in Figs. 9 and 7(a), validating the high sensitivity and resolution of the proposed LSPR biochemical sensor.

When solving partial differential equations, once a boundary condition has been set, all mathematical solutions are orthogonal; in other words, the mathematical solutions have an orthogonality of 1 only with themselves, and the orthogonality

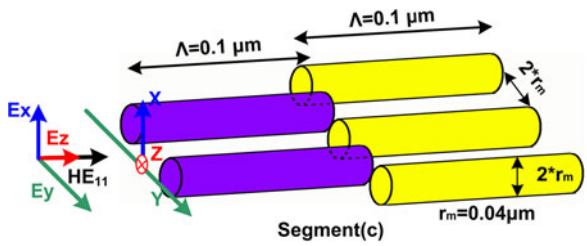

Fig. 9. Cylindrical nanometal array of HE_{11} in Segment (c), which was used to excite the LSPR wave.

between any two mathematical solutions is 0. However, because of limited server memory capacity and calculation time when performing numerical simulations, achieving an orthogonality of 0 is impossible; thus, errors are unavoidable when using the FEM. In this study, an error-verification mechanism previously proposed by the author [13], [36] was used (i.e., the meshing resolution used in the FEM must produce an orthogonality below –40 dB). The design and simulation process involved selecting a reasonable meshing resolution before calculating the numerical solutions (i.e., the modes). Subsequently, the orthogonality calculations were performed to determine whether the modes met the verification standard (i.e., whether the errors were within an acceptable range. In cases where the errors exceeded the range, the meshing resolution was increased and the procedure was repeated. For the proposed LSPR biochemical sensor, the meshing ratio of 1:8:160:1600 was used. Fig. 10 shows the orthogonality of 100 modes, verifying that a meshing ratio of 1:8:160:1600 satisfies the verification mechanism stipulating an orthogonality requirement of below –40 dB.

IV. Eigenmode Expansion Method

When designing the LSPR biochemical sensor, the EEM enabled the guided modes, which were obtained using the FEM, to transfer energy within the sensor components. The novel LSPR biochemical sensor contained a single-mode fiber component as well as a cylindrical nanometal array component with two cylindrical nanometal array arrangements. The EEM algorithm treated each component as a uniform waveguide with a fixed refractive index, in which each component was considered a segment. Segment (K–1) contacted Segment (K) at junction (J_{k-1}) [13], [36]–[42]. From a purely mathematical perspective, the EEM acted as a Fourier series expansion method, and every junction location in the sensor represented the area within which Fourier series expansion was performed. The Fourier series expansion principle posits that an insufficient number of expansion bases results in errors. Because of limited server memory capacity and calculation time when performing numerical simulations, including all of the modes (bases) is impossible. However, when an insufficient number of modes was used, power loss occurred every time the EEM was executed. Therefore, an error-verification mechanism previously proposed by the author was employed to test whether the number of modes in the EEM was sufficient to achieve a sensor energy consumption below –40 dB [13], [36]. During the design and subsequent simulations

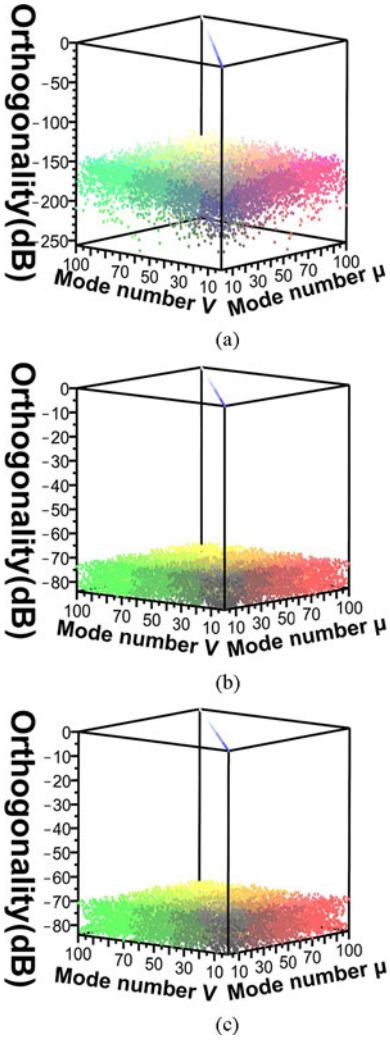

Fig. 10. Orthogonality between the 100 guided modes in Segments (a), (b), and (c).

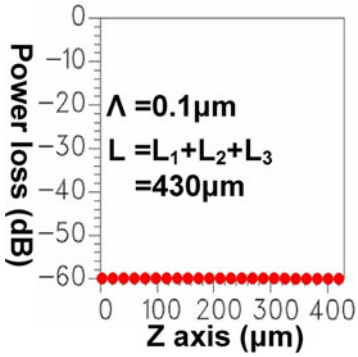

Fig. 11. The correlation between power loss and sensor length when using the EEM.

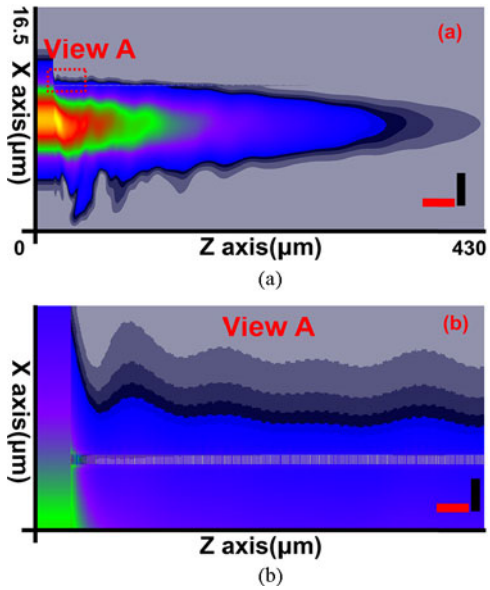

Fig. 12 (a) Power distribution map of the LSPR biochemical sensor excited by the HE_{11}; (b) enlarged view of "View A" from panel (a), in which the z- and x-axes were enlarged at a ratio of 37:430 and 23:220, respectively.

of the proposed LSPR biochemical sensor, an appropriate number of modes was selected, and calculations were performed to determine the overall energy consumption of the modes. The number of modes was increased if the energy loss failed to meet the accepted standard set by the verification mechanism, and the procedure was repeated until the errors were within an acceptable range. To design the novel LSPR biochemical sensor, 100 modes were used and the overall energy consumption was calculated (see Fig. 11). The results show that this number of modes was sufficient to satisfy the error verification standard (i.e., the overall energy consumption was less than –40 dB).

V. Design and Simulation

Based on the geometry of the novel LSPR biochemical sensor and adopting the theories described in Sections III and IV, four procedures and two verification mechanisms were proposed and applied to perform the numerical simulations and analyze the effectiveness of the proposed sensor. The procedures and verification mechanisms are described as follows: (1) locate 100 guided modes on the *x*-*y* plane using the FEM; (2) verify whether these guided modes have an overall energy consumption below –40 dB; (3) calculate the energy transferred by the 100 guided modes by using the EEM; (4) verify that the overall power loss when executing the EEM is below –40 dB; (5) produce an optical spectrum diagram for the LSPR biochemical sensor and calculate its resolution; and (6) analyze the ability of the sensor to detect changes in the refractive index of analytes based on the results from Step 5 [36]. To verify the sensitivity and resolution of the proposed LSPR biochemical sensor in exciting LSPR waves, the core mode depicted in Fig. 5 was used. Fig. 1 shows the incident LSPR wave that entered the sensor through the input terminal; subsequently, the transfer of energy by the sensor was calculated, the results of which are shown in Fig. 12(a). To enable clear observation of the LSPR wave from Fig. 12(a), the region marked as "View A" was enlarged and shown in Fig. 12(b). The enlargement ratio between Fig. 12(a) and (b) is 23:220 for the black and 37:430 for the red.

Using the spectral properties of the sensors enabled identifying the two critical indicators (i.e., sensitivity and resolution)

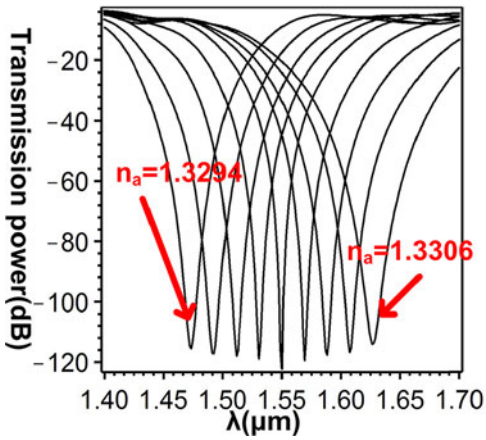

Fig. 13. Spectral curve of the novel LSPR biochemical sensor when the refractive index of the analyte was changed from $n_a = 1.3294$ to $n_a = 1.3306$.

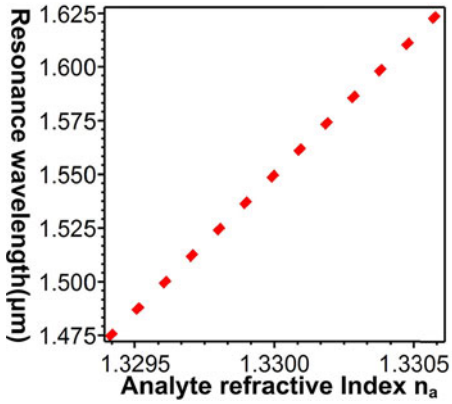

Fig. 14. Resonance wavelength curve of the novel LSPR biochemical sensor when the refractive index of the analyte was changed from $n_a = 1.3294$ to $n_a = 1.3306$.

for evaluating sensors. Subsequently, the energy transferred by the novel LSPR biochemical sensor was calculated by dividing the input energy by the output energy [13] (see Fig. 13). Fig. 13 shows the changes in spectral curve of the novel LSPR biochemical sensor as the refractive index of the analyte changes from $n_a = 1.3294$ to $n_a = 1.3306$. The results show that when the wavelength $\lambda = 1550$ nm, the sensor resolution was –120 dB. Based on the data in Fig. 13, the changes in the resonance wavelength of the sensor resulting from changes in the refractive index of the analytes can be easily detected and are depicted in Fig. 14, in which the resonance wavelength curve of the proposed LSPR biochemical sensor are shown when the refractive index of the analyte was changed from $n_a = 1.3294$ to $n_a = 1.3306$. The resonance wavelength of the proposed LSPR biochemical sensor increased from 1.473437 to 1.626562 μm. In other words, the sensitivity of the sensor was calculated, and the results are shown as follows:

$$\text{Sensitivity} \approx \frac{1.626562 - 1.473437}{1.3306 - 1.3294} \approx 127604 \left(\frac{\text{nm}}{\text{RIU}}\right). \quad (1)$$

When the electrons in nanometal materials absorb incident rays of a particular wavelength, collective oscillation occurs on the surface and between the nanometal particles. Compared with regular SPR sensors, which possess transmission ability, the proposed LSPR biochemical sensor possesses a higher number of resonance areas. This physical property enhanced the sensor's ability to detect changes in the analytes [13]. In other words, increasing the number of nanometal particles in the LSPR enhanced its sensitivity. Compared with the two current high-performance biochemical sensors, the novel LSPR biochemical sensor contained 320 050 (i.e., $(87 + 86) \times 1850$) particles and achieved a sensitivity of approximately 127 604 nm/RIU; the novel and high-performance LSPR biochemical fiber sensor containing 24 000 particles achieved a sensitivity of approximately 93987 nm/RIU) [13]; and the novel D-shape LSPR fiber sensor containing 1614 particles achieved a sensitivity of approximately 20 183.333 nm/RIU [22]. The simulation results show that the short length (approximately 430 μm), high resolution (approximately –120 dB), and high sensitivity (approximately 127 604 nm/RIU) of the novel LSPR biochemical sensor are advantageous.

VI. Conclusion

Because the improved FEM was faced with problems after integrating the PML and PRB, two innovative techniques (i.e., the OMM and BMM) were introduced in this study as a means to improve the meshing technique and to design the novel LSPR biochemical sensor. Such techniques involve dividing the sensors into four structure types according to their object boundary and size (i.e., small, medium, and large). With the area of the triangular elements used as a basis, the object boundaries, small objects, medium objects, and large objects were meshed at a ratio of 1:8:160:1600. Applying the described techniques markedly reduced the memory capacity and time spent performing calculations. Four procedures and two verification mechanisms were proposed and applied to perform numerical simulations and analyze the effectiveness of the proposed sensor. The results show that the proposed LSPR biochemical sensor not only outperformed two current high-performance biochemical sensors, but also featured advantages such as short length (approximately 430 μm), high resolution (approximately –120 dB) and high sensitivity (approximately 127 604 nm/RIU).

References

[1] N. Mohamed, D. Aurélien, E. K. Buntha, M. Julien, and C. Michael, "Angulo-spectral surface plasmon resonance imaging of nanofabricated grating surfaces," *Opt. Lett.*, vol. 35, no. 13, pp. 2209–2211, Jul. 2010.

[2] Y. F. Chau, Y. J. Lin, and D. P. Tsai, "Enhanced surface plasmon resonance based on the silver nanoshells connected by the nanobars," *Opt. Exp.*, vol. 18, no. 4, pp. 3510–3518, Feb. 2010.

[3] S. Moon, D. J. Kim, K. Kim, D. Kim, H. Lee, K. Lee, and S. Haam, "Surface-enhanced plasmon resonance detection of nanoparticle-conjugated DNA hybridization," *Appl. Opt.*, vol. 49, no. 3, pp. 484–491, Jan. 2010.

[4] W. C. Law, K. T. Yong, A. Baev, and P. N. Prasad, "Sensitivity improved surface plasmon resonance biosensor for cancer biomarker detection based on plasmonic enhancement," *ACS Nano*, vol. 5, no. 6, pp. 4858–4864, Apr. 2011.

[5] K. Koyo, "Model for measurement of water layer thickness under lipid bilayers by surface plasmon resonance," *Biomed. Opt. Exp.*, vol. 2, no. 5, pp. 1115–1120, Apr. 2011.
[6] P. Bhatia and B. D. Gupta, "Surface-plasmon-resonance-based fiber-optic refractive index sensor: Sensitivity enhancement," *Appl. Opt.*, vol. 50, no. 14, pp. 2032–2036, May 2011.
[7] Y. Zhang, H. Li, J. Duan, A. Shi, and Y. Liu, "Surface plasmon resonance sensor based on spectral interferometry: Numerical analysis," *Appl. Opt.*, vol. 52, no. 14, pp. 3253–3259, May 2013.
[8] A. Giorgini, S. Avino, P. Malara, G. Gagliardi, M. Casalino, G. Coppola, M. Iodice, P. Adam, K. Chadt, J. Homola, and P. De Natale, "Surface plasmon resonance optical cavity enhanced refractive index sensing," *Opt. Lett.*, vol. 38, no. 11, pp. 1951–1953, May 2013.
[9] C. Zhang, R. Wang, C. Min, S. Zhu, and X. C. Yuan, "Experimental approach to the microscopic phase-sensitive surface plasmon resonance biosensor," *Appl. Phys. Lett.*, vol. 102, p. 011114, Jan. 2013.
[10] A. P. Blanchard-Dionne, L. Guyot, S. Patskovsky, R. Gordon, and M. Meunier, "Intensity based surface plasmon resonance sensor using a nanohole rectangular array," *Opt. Exp.*, vol. 19, no. 16, pp. 15041–15046, Jul. 2011.
[11] M. Kumar and A. Kumar, "A simple and accurate method to analyze lossy optical waveguides: Applications to surface plasmon resonance based devices," *J. Lightw. Technol.*, vol. 32, no. 5, pp. 947–951, Mar. 2014.
[12] J. Li, D. F. Lu, Z. Zhang, Q. Liu, and Z. M. Qi, "Hierarchical mesoporous silica film modified near infrared SPR sensor with high sensitivities to small and large molecules," *Sens. Actuators B*, vol. 203, pp. 690–696, Nov. 2014.
[13] Y. J. He, "Novel and high-performance LSPR biochemical fiber sensor," *Sens. Actuators B*, vol. 206, pp. 212–219, Jan. 2015.
[14] S. W. Lee, K. S. Lee, J. Ahn, J. J. Lee, M. G. Kim, and Y. B. Shin, "Highly sensitive biosensing using arrays of plasmonic Au nanodisks realized by nanoimprint lithography," *ACS Nano*, vol. 5, no. 2, pp. 897–904, Jan. 2011.
[15] J. Zhu, W. Li, M. Zhu, W. Zhang, W. Niu, and G. Liu, "Influence of the pH value of a colloidal gold solution on the absorption spectra of an LSPR-assisted sensor," *AIP Adv.*, vol. 4, p. 031338, Mar. 2014.
[16] A. M. Lopatynskyi, O. G. Lopatynska, L. J. Guo, and V. I. Chegel, "Localized surface plasmon resonance biosensor—Part I: theoretical study of sensitivity-extended MIE approach," *IEEE Sens. J.*, vol. 11, no. 2, pp. 361–369, Feb. 2011.
[17] J. Yuan, H. Z. Cao, Y. Y. Xie, Z. X. Geng, Q. Kan, X. M. Duan, and H. D. Chen, "Gold elliptic nanocavity arrays biosensor with high refractive index sensitivity based on two-photon nanolithography," *IEEE Photon. J.*, vol. 7, no. 1, p. 4500108, Feb. 2015.
[18] S. S. Acimovic, M. A. Ortega, V. Sanz, J. Berthelot, J. L. Garcia-Cordero, J. Renger, S. J. Maerkl, M. P. Kreuzer, and R. Quidant, "LSPR chip for parallel, rapid, and sensitive detection of cancer makers in serum," *Nano Lett.*, vol. 14, no. 5, pp. 2636–2641, Apr. 2014.
[19] J. J. Giner-Casares and L. M. Liz-Marzan, "Plasmonic nanoparticles in 2D for biological applications: Toward active multipurpose platforms," *Nano Today*, vol. 9, no. 3, pp. 365–377, Jun. 2014.
[20] T. Allsop, R. Neal, M. Chengbo, K. Kalli, and D. Webb, "Highly sensitive, localized surface plasmon resonance fiber device for environmental sensing, based upon a structured bi-metal array of nano-wires," *Opt. Lett.*, vol. 39, no. 20, pp. 5798–5801, Oct. 2014.
[21] C. Li, Y. Li, Y. Ling, Y. Lai, C. Wu, and Y. Zhao, "Exploration of the growth process of ultrathin silica shells on the surface of gold nanorods by the localized surface plasmon resonance," *Nanotechnol.*, vol. 25, no. 4, pp. 045704–045711, Jan. 2014.
[22] Y. J. He, "Novel D-shape LSPR fiber sensor based on nano-metal strips," *Opt. Exp.*, vol. 21, no. 20, pp. 23498–23510, Sep. 2013.
[23] N. R. Jana, L. Gearheart, and C. J. Murphy, "Wet chemical synthesis of high aspect ratio cylindrical gold nanorods," *J. Phys. Chem. B*, vol. 105, pp. 4065–4067, 2001.
[24] S. Conesa-Boj, F. Boioli, E. Russo-Averchi, S. Dunand, M. Heiss, D. Riiffer, N. Wyrsch, C. Ballif, L. Miglio, and A. F. Morral, "Plastic and elastic strain fields in GaAs/Si core-shell nanowires," *Nano Lett.*, vol. 14, no. 4, pp. 1859–1864, Feb. 2014.
[25] S. J. Barrow, A. M. Funston, X. Wei, and P. Mulvaney, "DNA-directed self-assembly and optical properties of discrete 1D, 2D and 3D plasmonic structures," *Nano Today*, vol. 8, no. 2, pp. 138–167, Apr. 2013.
[26] C. E. Rubio-Mercedes, V. F. Rodriguez-Esquerre,, I. T. Lima, and H. F. Hernandez-Figueroa, "Design and chromatic aberration analysis of plasmonic lenses using the finite element method," *J. Lightw. Technol.*, vol. 31, no. 7, pp. 1114–1119, Apr. 2013.
[27] C. Ciminelli, C. M. Campanella, F. D. Olio, C. E. Campanella, and M. N. Armenise, "Lable-free optical resonant sensors for biochemical applications," *Progress Quantum Electron.*, vol. 37, no. 2, pp. 51–107, Mar. 2013.
[28] X. Huang and D. Zhang, "A high sensitivity and high linearity pressure sensor based on a peninsula-structured diaphragm for low-pressure ranges," *Sens. Actuators A*, vol. 216, pp. 176–189, Sep. 2014.
[29] Y. T. Duan, B. Chen, H. L. Chen, and Y. Yi, "Anisotropic-medium PML for efficient Laguerre-based FDTD method," *Electron. Lett.*, vol. 46, no. 5, pp. 318–319, Mar. 2010.
[30] A. Frangi, M. Cremonesi, A. Jaakkola, and T. Pensala, "Analysis of anchor and interface losses in piezoelectric MEMS resonators," *Sens. Actuators A*, vol. 190, pp. 127–135, Feb. 2013.
[31] J. Zhu and Y. Y. Lu, "Asymptotic solutions of eigenmodes in slab waveguides terminated by perfectly matched layers," *J. Opt. Soc. Amer. A*, vol. 30, no. 10, pp. 2090–2095, Oct. 2013.
[32] N. Tedeschi, F. Frezza, and A. Sihvola, "On the perfectly matched layer and the DB boundary condition," *J. Opt. Soc. Amer. A*, vol. 30, no. 10, pp. 1941–1946, Sep. 2013.
[33] X. Zhuansun and X. Ma, "Integral-based exponential time-differencing algorithm for the full-vectorial FDTD-PML analysis of PCF with material-dispersion," *IEEE Photon. Technol. Lett.*, vol. 24, no. 8, pp. 676–678, Apr. 2012.
[34] O. Ramadan, "DSP-PML algorithm for open region DNG meta-material FDTD simulations," *Electron. Lett.*, vol. 46, no. 1, pp. 16–18, Jan. 2010.
[35] Q. Lu, W. H. Guo, D. Byrne, and J. F. Donegan, "Leaky modes analysis in very deeply etched semiconductor ridge waveguides," *IEEE Photon. Technol. Lett.*, vol. 22, no. 6, pp. 407–409, Mar. 2010.
[36] Y. J. He, "Highly sensitive biochemical sensor comprising rectangular nanometal arrays," *Sens. Actuators B*, vol. 220, pp. 107–114, Dec. 2015.
[37] V. Krishnamurthy, K. Ravi, and S. T. Ho, "Analytical framework for the steady state analysis of wavelength-dependent and intensity-dependent interaction of multiple monochromatic beams in semiconductor photonic structures with multiple active and passive sections," *IEEE Quantum Electron.*, vol. 48, no. 10, pp. 1282–1299, Oct. 2012.
[38] G. B. Rusu, M. Asandulesa, I. Topala, V. Pohoata, N. Dumitrascu, and M. Barboiu, "Atmospheric pressure plasma polymers for tuned QCM detection of protein adhesion," *Biosens. Bioelectron.*, vol. 53, pp. 154–159, Mar. 2014.
[39] B. Fan, F. Liu, Y. Li, X. Wang, K. Cui, X. Feng, W. Zhang, and Y. Huang, "Integrated refractive index sensor based on hybrid coupler with short range surface plasmon polariton and dielectric waveguide," *Sens. Actuators B*, vol. 186, pp. 495–505, Sep. 2013.
[40] T. Scharf, D. Briand, S. Bühler, O. Manzardo, H. P. Herzig, and N. F. D. Rooij, "Miniaturized Fourier transform spectrometer for gas detection in the MIR region," *Sens. Actuators B*, vol. 147, no. 1, pp. 116–121, May 2010.
[41] N. Dalvand, T. G. Nguyen, T. L. Koch, and A. Mitchell, "Thin shallow-ridge silicon-on-insulator waveguide transitions and tapers," *IEEE Photon. Technol. Lett.*, vol. 25, no. 2, pp. 163–166, Jan. 2013.
[42] Y. J. He and X. Y. Chen, "Designing LPG-OADM based on a finite element method and an eigenmode expansion method," *IEEE Nanotech. Trans.*, vol. 12, no. 3, pp. 460–471, May 2013.

Yue-Jing He received the M.S. degree from the Department of Communication Engineering, National Chiao-Tung University, Hsinchu, Taiwan, in 2000, and the Ph.D. degree from the Department of Electrical Engineering, National Cheng Kung University, Tainan, Taiwan, in 2006. After graduation, he has been a Member of the faculty of the Electronic Engineering Department, National Chin-Yi University of Technology, Taichung, Taiwan, since 2008. His research interests include the areas of the component design in optical fiber communication and in surface plasmon resonance sensor.